1 On the dynamic response of reinforced concrete beams subjected to

2 drop weight impact

3 Joosef Leppänen[a,*], Morgan Johansson[a, b], Peter Grassl[c]

4 [a] Department of Architecture and Civil Engineering, Chalmers University of Technology, SE-

5 412 96 Göteborg, Sweden

6 [b] Norconsult AB, Göteborg, Sweden

7 [c] James Watt School of Engineering, University of Glasgow, Glasgow G128LT, UK

8 * Corresponding author. E-mail: joosef.leppanen@chalmers.se

9 Abstract

10 To improve the impact resistance of reinforced concrete structures, a detailed understanding of

11 the dynamic response is required. This study investigates this impact resistance using

12 experiments in combination with 3D non-linear finite element (FE) simulations. The

13 experiments made use of high-speed photography and digital image correlation (DIC), while a

14 damage-plasticity constitutive model for concrete was used in the FE simulations. Drop weight

15 impact tests of simply supported reinforced beams made of plain concrete and fibre reinforced

16 concrete were made, and it was shown that the addition of fibres reduced crack spacing, crack

17 widths and mid-point deflections. For the FE approach, tetrahedral elements were shown to be

18 well suited for capturing inclined shear cracks and the structural response obtained in

19 experiments and analyses agreed very well. The FE analyses showed that the reinforcement

20 strains were more localised for concrete with fibres, and hence predicted an increased risk of

21 reinforcement rupture.

22 *Keywords*: concrete, fibres, drop weight impact, digital image correlation (DIC), CDPM2

1. Introduction

Understanding the response of reinforced concrete structures subjected to impulse loading (i.e., blast and impact) is essential for designing critical infrastructure with confidence. Concrete cracking in tension, concrete crushing in compression, yielding of reinforcement, and interplay between concrete and reinforcement interact in a very short period, often resulting in a complex structural response. This response is difficult to predict without detailed experimental and numerical analyses.

The structural response of an impulse loaded structure may be very different compared to when subjected to a quasi-static load with the same geometric configuration. Due to the intense energy released in a short time, different phenomena will occur that affect both the material and structural response of the loaded structure. High strain rates cause the material in the structure to become stiffer, stronger, and more brittle [1–3], while wave propagation effects at the same time may greatly influence the structural response. Several studies [4–7] have noted that the load capacity increases with increased load rate. The load capacity increase is partly due to increased material strength as well as inertia effects causing a change in the structural response.

When a structure is subjected to a load, it takes time for this information to transfer within the structure. This time lapse is the case in all structures and for all types of loading. However, the information travels very fast within the structure (the shear wave velocity in concrete is approximately 2300 m/s; consequently, it is only when rapid loading is applied that such so called wave propagation effects will be important. In impact loading the impact force may be very high but with a short duration – in the order of just a few milliseconds or less. This means that all, or a large part, of the load may have been transferred to the structure before information of the load application has reached all parts of the structure. For example, in an impact loaded beam, there will be a notable lag in the time between impact and when the supports experience the applied load. This lag also means that the initial deformed shape of the beam will be very

2

48   different compared to the same beam subjected to a static point load. Since it takes some time

49   for the information of the applied load to reach all parts of the structure and it takes time for the

50   structure to react, parts of the beam will initially be 'unaware' of both the support conditions

51   and the applied load.

52   This initial response is denoted as the local response [8] and the deformed shape will vary as

53   schematically illustrated in Fig. 1 [9]. Here, a plastic hinge is assumed to form in the section of

54   impact and the affected part of the beam responds as if it was a fixed beam with an effective

55   span length l_{eff}. Consequently, tensile stresses that may cause cracks will form at the top of the

56   beam. The effective span length increases with time and, therefore the stiffness and load

57   capacity of the beam will vary during the local response. The time it takes for the initial response

58   to develop depends on the beam length and average force propagation velocity v_F. This velocity

59   is considerably smaller than the shear wave velocity and decreases approximately

60   proportionally with increased beam slenderness (approximately 250 to 1000 m/s for

61   length/depth of the beam varying between 10 and 4) [10,11]. Eventually, the effective length

62   reaches the supports. If the beam is not vertically restrained, it will briefly lift up due to the

63   inertia forces gathered within the effective length [12]. Once the whole beam is affected (i.e.,

64    $l_{eff} = l_{beam}$), the overall response [8] is initiated in which a deformed shape approximately

65   corresponding to that of static loading is obtained. However, this takes some time and until then

66   the beam's boundary conditions can be regarded as time-dependent fixed supports, where the

67   locations of these supports gradually move toward the free ends of the beam.
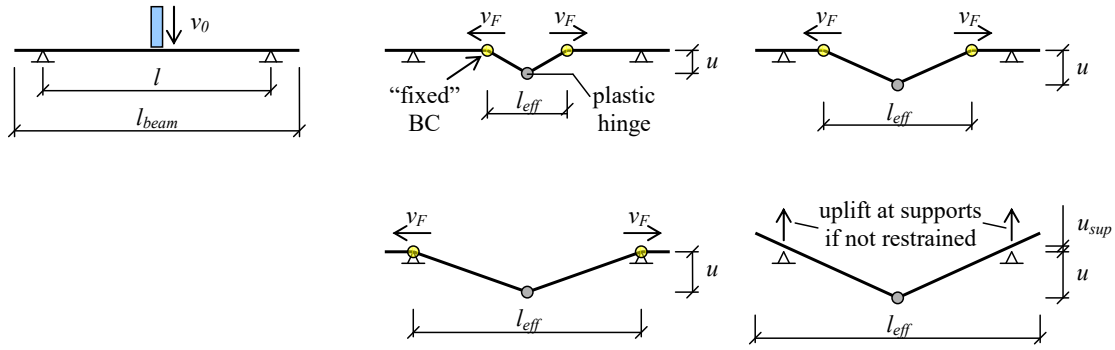
Fig. 1. Schematic illustration of how the deformed shape of an impact loaded beam develops during the local response. Based on [9] and [12].

The capacity of a structure to withstand the effect of impulse loading mainly depends on its ability to absorb the external energy applied by the load. Using a single degree of freedom model and assuming plastic impact, the external energy acting on the beam can be approximately determined as $W_e = m_w/(m_w + m_b) \cdot E_{k,0}$, where m_w is the mass of the drop weight, m_b is the effective mass of the beam, $E_{k,0} = m_w \cdot v_0^2/2$ is the kinetic energy of the drop weight at impact, and v_0 is the impact velocity [13]. Hence, the external energy applied to the beam will decrease with an increased beam mass. To withstand the effect of impact, the external energy should be balanced by the internal energy – $W_i = \int R(u) \, du$ – provided by the beam, where $R(u)$ is the load capacity as a function of the deflection u. Consequently, in an impulse-loaded structure, the internal energy W_i (not the maximum load capacity) is essential to withstand the load. In such structures it is usually preferred that the energy consumption of the structure is provided by large deformations rather than large internal forces [14–17]. This arrangement is ensured by designing the structure with regard to bending and providing it with a large plastic deformation capacity. To fulfil the latter criterion, the structure should be designed so it does not experience premature brittle failure, for example, due to shear. Hence, avoiding shear failure in an impulse-loaded structure is essential and has been the focus of several studies [18–20]. A potential problem here is that the mechanics of shear failure in impulse loaded structures are

4

88 not as well understood as failure due to bending [18] and several studies have noted that a

89 statically-loaded structure that fails due to bending may instead fail in shear when subjected to

90 impulse loading [18–20].

91 In the equation for the external energy, the mass of the impacting body is important. However,

92 the impacting body's geometric properties are also important and as such have been the subject

93 of several studies [21–25]. These studies have concluded that an increased radius on the drop

94 weight head results in increased contact stiffness, that this stiffness significantly influences the

95 impact force (force increase with increased stiffness), and that a decreased head radius leads to

96 more severe local concrete damage at the impact zone. However, the contact stiffness has only

97 minor effect on the resulting impulse, impact energy, and resulting mid-span displacement of

98 the loaded structure. Furthermore, a flat head is sensitive to the inclination angle of the drop

99 weight [24], suggesting that it is preferable to use a head with a radius that is not too large.

100 If the beam's internal energy capacity is high enough (i.e., $W_i \geq W_e$), the structure can withstand

101 the effect of impulse loading and reach its maximum deformation when $W_i = W_e$. However, due

102 to elastic energy gathered in the structure, it will rebound in the opposite direction of the load,

103 and the beam will lose contact with its supports if it is not restrained. Consequently, restrained

104 boundary conditions may greatly affect the response of the rebounded beam, although it will

105 have negligible effect on the response up to maximum deformation in the direction of the

106 applied load.

107 Simplified calculation tools, based on spring-mass models of one or several degrees of freedom,

108 are commonly used in practical design of impulse-loaded structures [15–17,26]. Such tools are

109 advantageous in the sense that they provide an improved understanding to the fundamental

110 physics behind complex events such as impact-loaded structures. Furthermore, they are fast and

111 therefore may be very powerful since, once defined, it is easy to make many calculations

112   quickly. The improvement of such simplified methods is also the subject of several studies

113   [8,9,23]. However, to understand in detail what happens during impact loading, more detailed

114   models – e.g., FE models using 3D continuum elements – may be needed that correctly describe

115   more complex phenomena such as concrete cracking and crushing, reinforcement yielding, and

116   loss of bond. Although such tools are potentially powerful, experiments are still needed to check

117   whether the FE results correspond to experimental results. Therefore, FE analyses should be

118   regarded as a complement to experiments; that is, even if both methods have their advantages

119   when used alone, they are even more powerful when used together. In the present study,

120   reinforced beams of plain and fibre reinforced concrete subjected to impact loading were tested.

121   The test set-up was designed for the specimens to obtain a bending mode response and to avoid

122   shear failure with the purpose to use these results as a benchmark for nonlinear FE analyses.

123   Drop weight impact tests have been widely used to experimentally investigate the response of

124   concrete beams [8,18,19,27–34] recorded in the form of global quantities such as impact force,

125   support reaction force, midspan deflections, and final crack patterns. Recently, digital image

126   correlation techniques (DIC) [35] have been used to investigate the evolution of crack patterns

127   in impact tests of concrete beams reinforced with traditional steel bars (RC) [10,36]. This

128   technique makes it possible to reproduce the strain field on the concrete surface and therefore

129   provide improved understanding of the dynamic response of the loaded structure. Here, DIC

130   was used to monitor the crack evolution of RC and steel fibre reinforced concrete beams

131   reinforced with traditional steel bars (FRC). This experimental study provides in depth

132   information about the response of concrete subjected to impact loading and a benchmark for

133   evaluating the performance of numerical modelling.

134   Numerical modelling approaches for evaluating the detailed nonlinear response of concrete

135   structures subjected to impact loading are commonly based on the finite element method, which

136   is used to model concrete and steel reinforcement as interacting phases. For concrete, models

137 for cracking and crushing are commonly based on plasticity [37,38], damage mechanics

138 [39,40], or combinations of these two [41–45]. Alternative approaches include micro-plane

139 based models [46,47] and discrete methods [48,49].

140 FE analyses use an implicit or explicit solution method [50]. In the implicit method, equilibrium

141 is based on information in both the current and previous increments, so that an iteration

142 procedure is needed to find the equilibrium. In the explicit method, the equilibrium in the

143 current increment is based solely on information in previous load increments, and therefore, an

144 iteration procedure is not required. Hence, using an explicit method may be an effective way to

145 avoid numerical convergence problems encountered when using an implicit method to solve

146 nonlinear problems. However, with the explicit method very small time steps have to be used

147 to obtain a stable solution. When modelling impact loading, small time steps are anyway needed

148 to correctly capture the response. Consequently, an explicit solution method is suitable to model

149 impact loading.

150 Here, in the numerical analyses, the damage-plasticity model CDPM2 proposed by the third

151 author [51,52], and implemented in LS-DYNA as *MAT_CDPM (*MAT_273), was used as

152 the concrete constitutive model. This model reproduces many of the key characteristics of

153 concrete – e.g., softening in tension and low confined compression with reduction of stiffness

154 and permanent strains, and pressure sensitive strength and deformation capacity for triaxial

155 compression [51]. This model also reproduces the strain rate dependence of concrete, which is

156 important for modeling the dynamic response of structures [52].

157 In LS-DYNA, several different types of damping are available; e.g. Rayleigh damping and

158 artificial bulk viscosity. The former method is a mass and stiffness proportional viscous

159 damping that presents a common approach to simulate the energy dissipation in structural

160 dynamics, while the latter is a method used to handle discontinuous shock waves in materials.

161 In an impulse loaded structure, it is usually the initial response that is of interest; i.e. the peak

162   deformation. Hence, the effect of mass weighted damping is small and can often be neglected

163   [14]. However, for structures subjected to very high strain rates (>10 s^{-1}), e.g. high-speed

164   projectiles impact on concrete slabs, it has in [53] been shown that the bulk viscosity can have

165   a significant influence on the resulting projectile penetration depth. There, it is also argued that

166   bulk viscosity, due to both physical aspects and numerical reasons, must be included in the

167   analysis. This statement, though, is contradicted by [54], where it is instead argued that bulk

168   viscosity should not be included but an enhanced constitutive model should be used. For

169   impulse loading of RC and FRC structures, it is common to use hexahedral elements in the

170   numerical model in the FE program LS-DYNA [24,55–58]. However, it is well known that the

171   element type affects the crack patterns [59,60]. It was shown that the use of tetrahedral elements

172   made it easier to follow diagonal shear cracks. In addition, CDPM2 has been shown to perform

173   well for quasi-static loading with tetrahedral elements [61]. Studies using tetrahedral elements

174   for dynamically loaded concrete structures have been carried out in LS-DYNA and other FE

175   programs [62–64]. Response of steel fibre reinforced concrete to impact and blast loading can

176   be predicted accurately using tetrahedral elements in three-dimensional numerical studies [62].

177   A model based on continuum mechanics, rate dependent microplane, and standard tetrahedral

178   finite elements has accurately predicted the complex dynamic fracture process of concrete [63].

179   Similarly, using tetrahedral elements can predict tension-shear damage and mixed-mode

180   fracture in solids subjected to dynamic loading [64]. Merging the material model CDPM2 with

181   tetrahedral elements has satisfactorily reproduced impact loading with respect to the bond

182   between steel bars and concrete, merged and coincident with slip [13]. Compared to hexahedral

183   elements, tetrahedral elements in LS-DYNA with CDPM2 seem to capture better diagonal shear

184   cracks due to impact loading [65]. However, these studies neglect the strain rate effects both

185   for the concrete and the steel bars [13,65].

186   This paper investigates the difference in results when using hexahedral and tetrahedral elements

187   for RC and FRC structures subjected to impact loading when using the previously developed

188   material model CDPM2, including strain rate effects (for concrete and steel rebar). Drop weight

189   (made of steel) impact tests were carried out on plain concrete and fibre reinforced concrete

190   beams with ribbed steel bars. A combination of high-speed photography and DIC made it

191   possible to compare these drop weight test results of crack patterns and structural response with

192   FE analyses. The aim of this comparison was to find whether CDPM2 can sufficiently model

193   impact loaded RC and FRC structures and to use CDPM2 to study phenomena that are difficult

194   to extract from experiments only, such as reinforcement strains. Specifically, CDPM2 was used

195   to study the effect of strain localisation and development of plastic hinge in an impact-loaded

196   structure made of fibre-reinforced concrete and plain concrete.

197   **2. Experimental test set-up**

198   In the present study, a 10.1 kg drop weight, released from a height of 5.5 m, impacted simply

199   supported beams placed on rollers (Fig. 2). The test specimens were small: the length of the

200   beams was 1.18 m, the length of the span was 1.0 m, and the beam cross section was

201   0.1 x 0.1 m. The beam height corresponds to a height of a slab in, e.g., a Swedish civil defence

202   shelter with a scale factor of 1:3.5. The beams were reinforced with 2+2 ribbed steel bars with

203   a nominal diameter of 6 mm resulting in a reinforcement ratio of about 0.7 %. The roller

204   supports had a diameter of 70 mm and were free to roll against their supports, which were made

205   of thick steel plates. The beams were not restrained, so during the test the beam could obtain a

206   rigid body movement upwards once rebounding occurred – i.e., the beam's boundary conditions

207   were not the same for downward and upward deformation. The main reason for this test set-up

208   was to avoid restraint moments. This was deemed to be an acceptable solution since the purpose

209   here was to study the beam's structural response when deforming in the direction of the applied

210   load (i.e., downward). This configuration also made it easy to correctly position the beams in

211   the test set-up, providing for an effective testing procedure with good repeatability. No impact

212   or reaction forces were measured.

213   A beam is normally restrained at the connections, and in impact tests typically an upper restraint

214   is added to the supports to prevent rebounding [8,18,19,28,31]. However, in impact tests

215   simplify support conditions are also often used, by using only simply supported beams without

216   an upper restraint [30,32–34], and some studies have used both upper restrained and

217   unrestrained beams [27,29]. Simply supported boundary conditions cannot capture the rebound

218   effect. Typically, the initial deflection causes the most damage and therefore is the most

219   dangerous. Furthermore, small scale experiments are commonly used for impact tests – small

220   cross sections, e.g., 0.1 m x 0.1 m [27,32,33] or 0.15 x 0.15 m [29,34] and span lengths up to

221   1.0 m.

222

223   (a)   b)
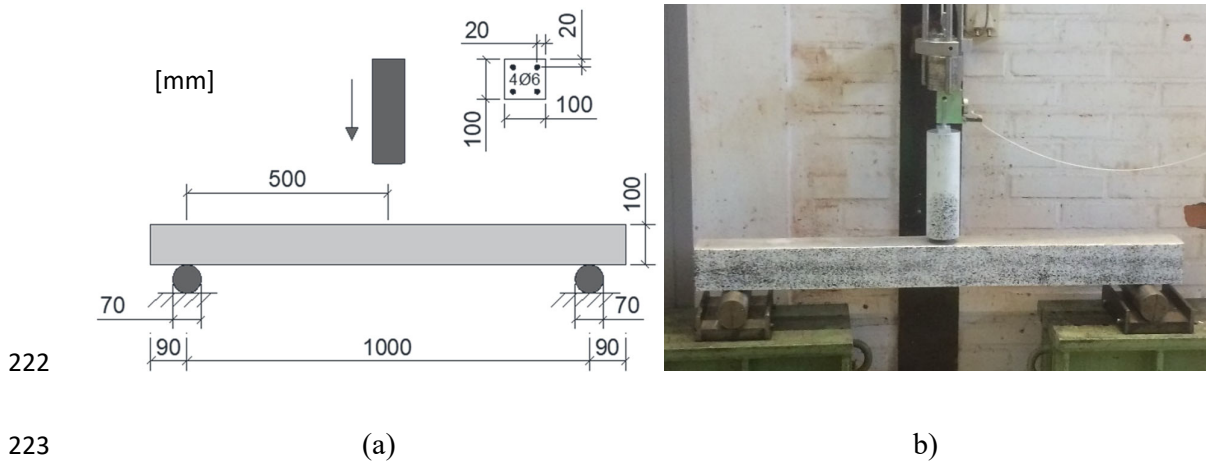
224   **Fig. 2.**   Experimental test set-up: (a) geometry, and (b) photo of beam and drop weight

225   with speckled pattern applied.

226   The experiments analysed in this paper were part of a larger experimental series [12,36]. From

227   this series of experiments, five RC and four FRC beams were selected for the present

228   investigation.

229   A high-speed camera was used during the drop weight impact tests. Images were taken every

230   0.2 ms (i.e., 5000 frames per second, fps). This frame rate is not high enough to capture what

231   happens locally in the impact zone, but it is accurate enough to obtain information about the

232   global response of the beam and its crack propagation. Only half of the beam was recorded to

233   obtain good resolution. DIC with the software GOM Correlate ARAMIS [66] was used to

234   analyse the high-speed camera images. This technique is commonly used to measure

235   deformations and strain fields of a surface. The basic idea is to analyse the change of a surface

236   speckle pattern in a series of digital images taken during the test. This analysis is done by

237   tracking the position of discrete pixel subsets of the speckle pattern. If the time between each

238   image taken during the test is known, the deformations, strains, velocities, and accelerations

239   can be measured. To create the surface component in GOM Correlate, a facet size of 15 pixels

240   and a point distance of 10 pixels were used for the RC beam. For the FRC beam, a facet size of

241   15 pixels and a point distance of 5 pixels were used. Each pixel had a point distance of

242   approximately 0.6 mm in GOM Correlate. DIC was used for all beams tested to determine crack

243   patterns, deformed shape and midpoint-deflection. In addition, DIC was used to determine that

244   the average impact velocity of the drop weight was 10.35 m/s.

245   The specimens were cast with self-compacting concrete (Table A.1). The fibre reinforced

246   concrete, 40 kg/m^3 ($V_f = 0.5$ %) of Dramix steel fibres, was 35 mm long and 0.55 mm in

247   diameter. The compressive strength f_c and tensile strength f_t and fracture energy G_F were tested

248   according to standard procedures [67–70].

249   For the plain concrete, wedge splitting tests [69] were used to determine the fracture energy.

250   For the fibre reinforced concrete, RILEM beams were tested according to [70], and the force

251   and crack mouth opening displacement (CMOD) were recorded (Fig. A.1).

252 Material testing on the day of the impact experiments (45 days after casting) gave the following

253 mean values for the three test specimens for each test: f_c = 45.5 (49.7) MPa,

254 f_t = 3.28 (3.55) MPa; and G_F = 113 (1676) Nm/m^2. The values given refer to RC (FRC).

255 Material tests for the reinforcement were also conducted. The reinforcement was coil

256 reinforcement of class C [71] with a characteristic yield strength of 500 MPa. The stress-strain

257 curve for the tested reinforcement bars are shown in Fig. A.2. The data for the drop weight used

258 in the experiments are shown in Table A.2.

259 **3. FE analyses**

260 **3.1 Concrete constitutive model**

261 The previously developed concrete damage-plasticity model 2 (CDPM2) [42,51,52] was used.

262 This constitutive model can reproduce many features of the failure process of concrete, which

263 are important for modelling structures subjected to impact loading. The model has been shown

264 to accurately reproduce the effect of confinement on strength and strain capacity in

265 compression, which is important for capturing the effect of lateral confinement generated below

266 the impact point. The model can describe the stiffness change for a transition from tension to

267 compression and vice-versa, which occurs often in dynamic simulations due to the effect of

268 wave propagation and reflection. In addition, the model describes the dependence of tensile and

269 compressive strength on strain rate [52].

270 The techniques in CDPM2, which can capture these features, are outlined briefly. In CDPM2,

271 the stress evaluation is based on a combination of damage mechanics and elasto-plasticity. With

272 respect to plasticity, the effective stress in the undamaged material is determined. The damage

273 is then used to evaluate the nominal stress by applying tensile and compressive damage

274 variables to positive and negative parts of the principal effective stress, respectively.

275 The plasticity part of the model is formulated in the effective stress space by means of the

276 Haigh-Westergaard stress coordinates, which are the volumetric effective stress $\bar{\sigma}_v$, the length

12

277   of the deviatoric effective stress $\bar{\rho}$ and the Lode angle $\bar{\theta}$ [72]. The yield surface is based on an

278   extension of the static strength envelope [73], which was shown to reproduce experimental

279   results well. This strength envelope is characterised by curved meridians and deviatoric sections

280   varying from almost triangular in tension to almost circular in highly confined compression

281   (Fig. 3).

282

283   (a)   (b)
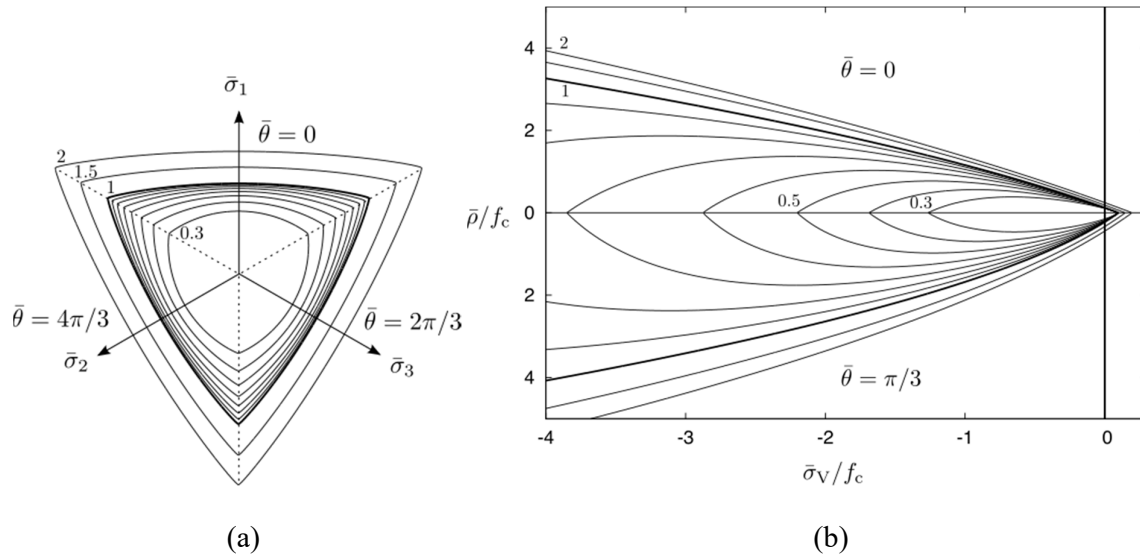
284   **Fig. 3**.   Evolution of the yield surface for varying values of the hardening variable q_h

285   (from 0.3 to 2), which is smaller than 1 in the pre-peak and larger than 1 in the post-peak regime:

286   (a) deviatoric section for a constant volumetric stress of $\bar{\sigma}_v = -f_c/3$ and (b) meridians at $\bar{\theta} = \pi/3$

287   (compression) and $\bar{\theta} = 0$ (tension). A thicker line indicates static strength surface where $q_h =$

288   1.

289   Based on this static strength envelope, static pre- and post-peak regimes were defined. In the

290   pre-peak regime, the yield surface is capped both in hydrostatic tension and compression. At

291   peak, the static strength envelope previously proposed in [73] is reached, which is open in

292   hydrostatic compression. In the post-peak regime, the yield surface further extends with the

293   shape being similar to the strength envelope. The hardening in the post-peak regime is

294   controlled by the hardening modulus H_p. The greater the value of H_p, the smaller the

295   contribution of plasticity in the post-peak regime.

296   In quasi-static simulations, damage is initiated once the strength envelope is reached. For

297   dynamic simulations in which the strain rate dependence of concrete is considered, damage

298   initiation is made dependent on the strain rate: the greater the strain rate, the greater the delay

299   of the damage initiation [52]. This is achieved by dividing the rates of the equivalent strains by

300   a strain rate dependent factor which is equal to one for quasi-static loading and increases with

301   increasing strain rate. This way to model the rate dependence of strength is a simplified version

302   of the often used damage delay approach [74–76]. A visco-elastic model to describe the rate

303   dependence of the elastic response as used, for instance, in [75,77] was not considered in this

304   study. Consequently, there is no damping in the analyses due to sudden changes in strain rate

305   as they occur during cracking. Consequently, the strength at which damage (and softening) is

306   initiated exceeds the static strength of the envelope (Fig. 4). This means that for dynamic

307   loading, the pre and post-peak regimes differ from those defined by the static strength envelope.

308   For this technique to produce reasonable results in the pre-peak in compression, H_p must be set

309   to a large value so that the plastic strain before the onset of damage remains small. Therefore,

310    $H_\mathrm{p} = 0.5$ was used. The effect of strain rate on compressive and tensile strengths were modelled

311   using equations proposed in Model Code 1990 [78] and [2]. All the equations used in CDPM2

312   for modelling the strain rate effect are shown in [52] in detail.

313   Once damage is initiated, the response is a combination of the theory of plasticity and damage

314   mechanics. Evolution laws for tensile and compressive damage are formulated as functions of

315   positive and negative parts of the principal effective stress so that tensile and compressive

316   softening responses can be described independently. Mesh-independent results are obtained

317   using the crack-band approach [79]. In this approach, the function for the tensile damage

318   variable is derived from a bilinear stress-crack opening (σ - w_c) curve, so the results of analyses

319   of tensile failure in which strains localise in mesh-dependent regions are independent of the

320   finite element mesh [79–81]. Consequently, the finer the mesh, the larger the strain at constant

321   crack opening. If the strain rate in cracked elements were used, a strong mesh-dependence

322   would be obtained, because, in the crack band approach, for a constant crack opening the strain

323   is a function of the element size. Therefore, once damage is initiated in a material point, the

324   strain rate effect on strength is set constant to the value reached in that time step.

325

326   (a)   (b)
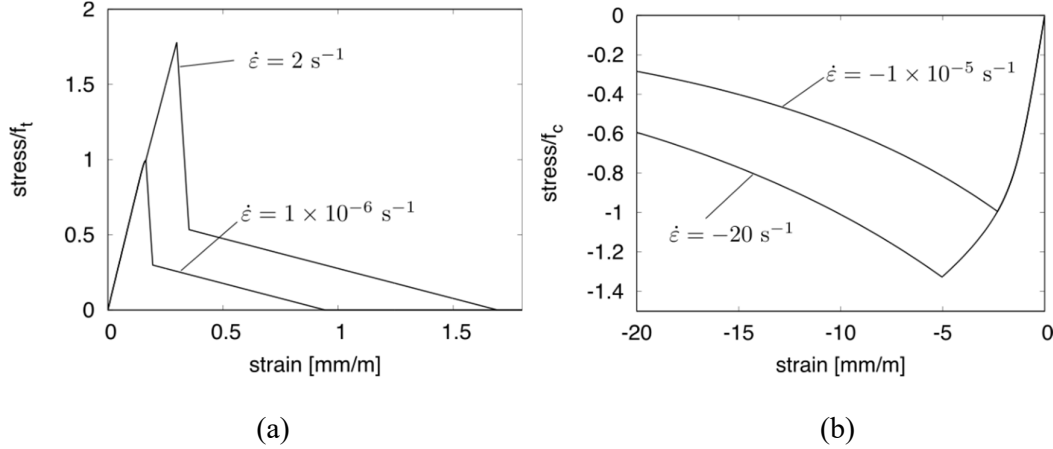
327   **Fig. 4**   Effect of strain rate on softening responses used to determine damage variables:

328   (a) bilinear stress-crack opening curve used to determine tensile damage variable and (b)

329   exponential stress-inelastic strain curve used to evaluate the compressive damage variable.

330   The tensile fracture energy of concrete G_F is defined as the area under the stress-crack opening

331   curve for quasi-static loading (strain rate factor equal to one). For the present bilinear curve,

332   this results in $G_F = (f_t w_{fl} + f_{t1} w_f)/2$. For the default in CDPM2, $f_{t1} = 0.3 f_t$ and $w_{fl} = 0.15 w_f$, so

333   $G_F = 0.225 f_t w_f$. Thus, the crack opening threshold is related to the area under the stress-crack

334   opening curve (fracture energy) as $w_f = 4.444 G_F/f_t$. Within the crack band approach in CDPM2,

335   the crack opening w_c is converted into an inelastic strain $\varepsilon_c = w_c/h_b$, where h_b is the assumed

336   width of the band in which strains localise. For linear hexahedral elements with reduced

337   integration used in this study, the band width is set to $h_b = \sqrt[3]{V_e}$, where V_e is the element

338   volume. For linear tetrahedral elements, the band width is $h_b = 1.79\sqrt[3]{V_e}$. This practical

339   approach produces similar global energy dissipations for tetrahedral and hexahedral meshes

340   [61], which was acceptable for the present comparison. More refined approaches in which the

15

341 band width is determined based on principal directions of stresses and/or strains have also been

342 presented [82].

343 The compressive damage variable is linked to a stress-inelastic strain curve, since the

344 deformation patterns in the compressive zones of applications dominated by bending are often

345 mesh-size independent [51].

346 CDPM2 requires many input parameters, which can be divided into groups related to the elastic,

347 plastic and damage parts of the model. In the present work, most of these parameters are set to

348 their default values as described, where it was shown that these parameters provide a good

349 match with experimental results for quasi-static loading [51]. Some of the parameters are

350 directly linked to experimental results, such as the f_t and f_c (Section 2). Young´s modulus was

351 calculated according to EN 1992-1-1 [71] as $E_{cm} = 22 \cdot (f_{cm}/10)^{0.3}$, and the density ρ was set to

352 2400 kg/m³. The damage threshold w_f was adjusted to match material data available for the

353 different groups of analyses. For plain concrete, w_f was calculated using the fracture energy

354 stated in Section 2. For fibre reinforced concrete, three point bending tests were performed as

355 described [70]. Then, inverse analysis was used to determine the input parameters for the

356 bilinear stress-crack opening law in CDPM2 (Fig. A.1). In CDPM2, the default value of the

357 inelastic strain threshold ε_{fc} results in a very brittle response in compression. To avoid

358 numerical difficulties, it is sometimes required to choose a more ductile compressive response

359 to avoid premature failure in regions close to supports or applied loads. Therefore, for

360 tetrahedral meshes, this parameter was set to $\varepsilon_{fc} = 0.001$, whereas for hexahedral meshes the

361 default $\varepsilon_{fc} = 0.0001$ was used.

362 **3.2 Reinforcement constitutive model**

363 The material model Johnson-Cook [83] was used to describe the stress-strain response of the

364 reinforcement steel. The yield stress is expressed as follows:

365 $\sigma = (A + B \cdot \varepsilon_p^n)(1 + C \cdot \ln \dot{\varepsilon}^*)(1 - T^{*m})$,

16

366   with five material constants: A, B, n, C and m. Here, ε_p is the equivalent plastic strain, $\dot{\varepsilon}^* = \dfrac{\dot{\varepsilon}}{\dot{\varepsilon}_0}$

367   is the dimensionless plastic strain rate and T^* is the dimensionless temperature.

368   The constants A, B, and n (expression in the first set of brackets) give the stress as a function of

369   strain for $\dot{\varepsilon}^* = 1$ and $T^* = 0$, which correspond to the static material tests. The input material

370   parameters of the model ($A = 400$ MPa, $B = 450$ MPa and $n = 0.21$) were chosen by fitting

371   material tests of the reinforcement bars (Fig. A.2). The strain rate was modelled per previous

372   recommendations [84], with quasi-static threshold strain rate $\dot{\varepsilon}_0 = 10^{-4}$ and the strain rate

373   constant $C = 0.017$. Temperature effects were not considered in the FE analyses.

374   There was no need to model rupture of the reinforcement as the effective plastic strains were

375   expected to be smaller than the ultimate strain. The analyses used the following values:

376    $E = 200$ GPa, Poisson's ratio $\upsilon = 0.3$ and $\rho = 7850$ kg/m^3.

377   **3.3 Numerical model**

378   Three-dimensional numerical analyses of the drop weight impact test were conducted using the

379   software LS-DYNA [85]. An explicit method based on central difference scheme [85] with an

380   automatic time step control was used in the numerical analyses. The time step was in the order

381   of $3.5 \cdot 10^{-4}$ ms and $2.3 \cdot 10^{-4}$ ms for hexahedral and tetrahedral elements, respectively. Default

382   values in LS-DYNA [85] were used for both Rayleigh damping (no damping) and artificial bulk

383   viscosity (1.5 for quadratic and 0.06 for linear viscosity coefficients). For the impact tests

384   studied, the maximum strain rate was in the order of about 1-10 s^{-1}, and therefore bulk viscosity

385   was not expected to influence the results from the FE analyses. A sensitivity analysis was

386   performed, which confirmed this expectation.

387   The model consisted of four parts: the roller supports, the concrete beam, reinforcement

388   embedded in the concrete beam, and the drop weight (including the radius of the head), see

389   Fig. 5. For the beams and the supports, solid hexahedral and tetrahedral elements were used.

390   The hexahedral and tetrahedral elements were 8-node and 4 node solid elements, respectively,

391   with one integration point. The drop weight was modelled with hexahedral mesh. The

392   reinforcement was modelled with beam elements using Hughes-Liu formulation [85] with

393   circular cross section. Hourglass control was needed to ensure stability of hexahedral elements,

394   and the Belytschko-Bindeman formulation [85] was used with default input parameters.

395   Convergence of the element size was previously studied for the hexahedral and tetrahedral

396   meshes, with element edge lengths of one side of 2.5 mm (only for hexahedral), 5 mm, 10 mm,

397   and 20 mm [65]. In this study, the same geometries of the beam and drop weight were used; the

398   drop heights, though were different (2.5 m and 5.0 m). It was concluded that an element edge

399   length of 5 mm for both hexahedral and tetrahedral mesh were adequate to accurately represent

400   the deflections and crack patterns. Thus, in this study an element length of 5 mm for both

401   element types was chosen, which resulted in about 100000 elements and 900000 elements for

402   the beam with hexahedral elements and tetrahedral elements, respectively.

403   To simulate the simply supported boundary conditions, rollers were fixed at the bottom and an

404   automatic surface to surface contact, based on Taylor and Flanagan [85], without friction was

405   used between the drop weight and the concrete beam. The same contact definition was used

406   between the beam and the rollers.

407   The reinforcement was modelled with 5 mm beam elements assuming perfect bond between

408   reinforcement and concrete, which has been shown to provide acceptable results [13]. The same

409   nodes were used for concrete and reinforcement elements for both FE models.

410   The drop weight and the roller supports were modelled to be elastic: $E = 200$ GPa and $\upsilon = 0.3$.

411   A small hole was drilled in the drop weight where an accelerometer (not used in the tests) was

412   attached. This hole was not included in the FE model. Hence, to account for this, the steel

413   density of the drop weight was adjusted so that the mass corresponded to the mass in the

414   experiments ($\rho = 7753$ kg/m^3).

415

416   (a)   (b)   (c)
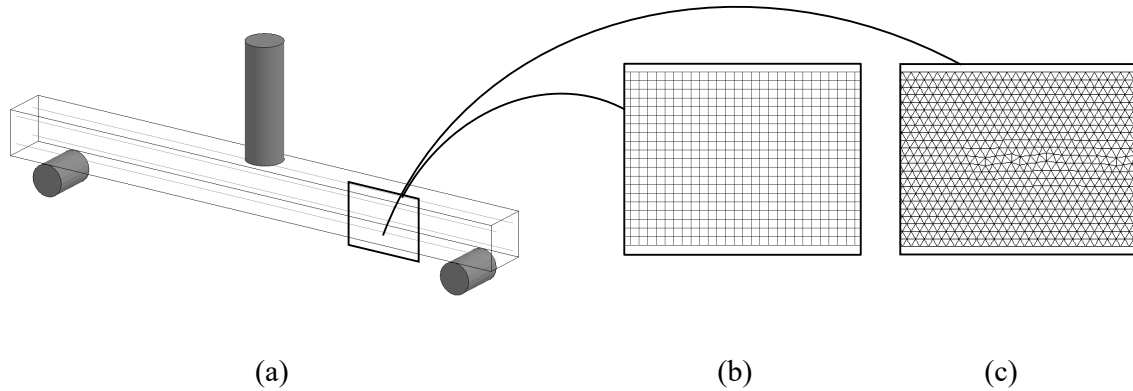
417   **Fig. 5.**   Numerical model used in the FE analyses: (a) 3D model, (b) hexahedral mesh,

418   and (c) tetrahedral mesh.

419   **4. Results**

420   The midpoint deflections obtained from DIC and FE analyses for RC and FRC beams are

421   compared with experimental results (5 RC and 4 FRC) in Fig. 6; dashed lines in the figure

422   indicate the beams used to compare crack patterns in Fig. 7 and Fig. 8 and the initial relative

423   deformation in Fig. 9. This comparison shows that in general the beam deflections can be

424   modelled effectively using CDPM2. However, the maximum midpoint deflection is

425   overestimated using hexahedral elements. For the drop weight tests with RC beams, the

426   maximum midpoint deflections were between 21 and 25 mm, with an average value of about

427   23 mm and in the FE analysis the maximum midpoint deflection was 29 mm using hexahedral

428   elements. However, when using tetrahedral elements, the maximum midpoint deflection was

429   25 mm, which is very close to the experimental results.

430   For the FRC beams, it was found that the addition of fibres decreased the maximum midpoint

431   deflection; and in the tests the maximum midpoint deflections were between 18 and 20 mm,

432   with an average value of 19 mm. In the FE analysis, the maximum midpoint deflection was

433   25 mm and 22 mm using hexahedral and tetrahedral elements, respectively.

(a)   (b)
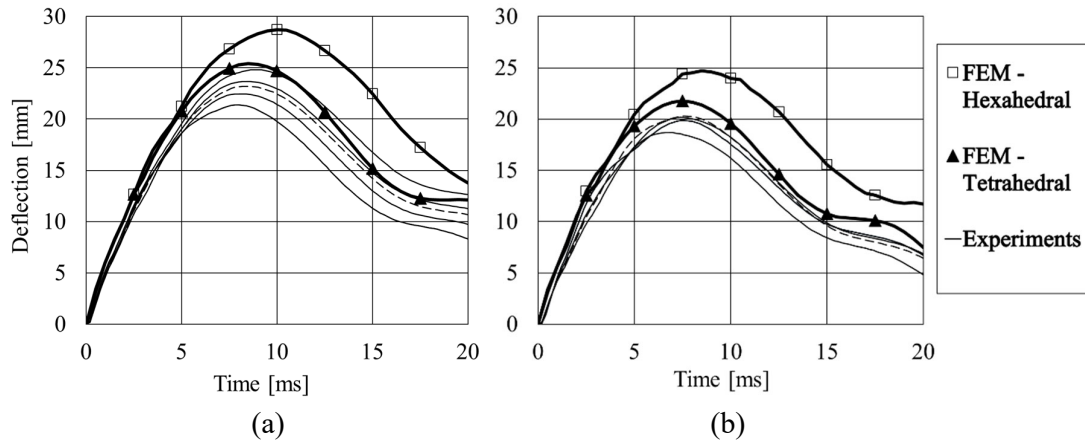
434 **Fig. 6.**   Deflection in the midpoint of the beams, comparison with experiments (5 + 4

435   beams) and FE analyses using hexahedral and tetrahedral elements, (a) RC beams,

436   and (b) FRC beams. Dashed lines correspond to the experimental beams used to

437   compare crack patterns in Fig. 7 and Fig. 8 and initial relative deformation in

438   Fig. 9.

439   DIC made it possible to study the crack propagation as a function of time in the experiments.

440   Here, just two beams from the experiments, one for RC and one for FRC, are presented. In

441   Fig. 7, DIC and FE show the crack patterns at an initial stage and the stage at maximum

442   deflection. In the DIC analyses, black indicates a crack visible to the eye (approximately

443   0.1 mm). In the numerical analyses the maximum principal strains were plotted and black

444   corresponds to the cracking strain: $\varepsilon_{crack} = 0.017$ (for tetrahedral elements).

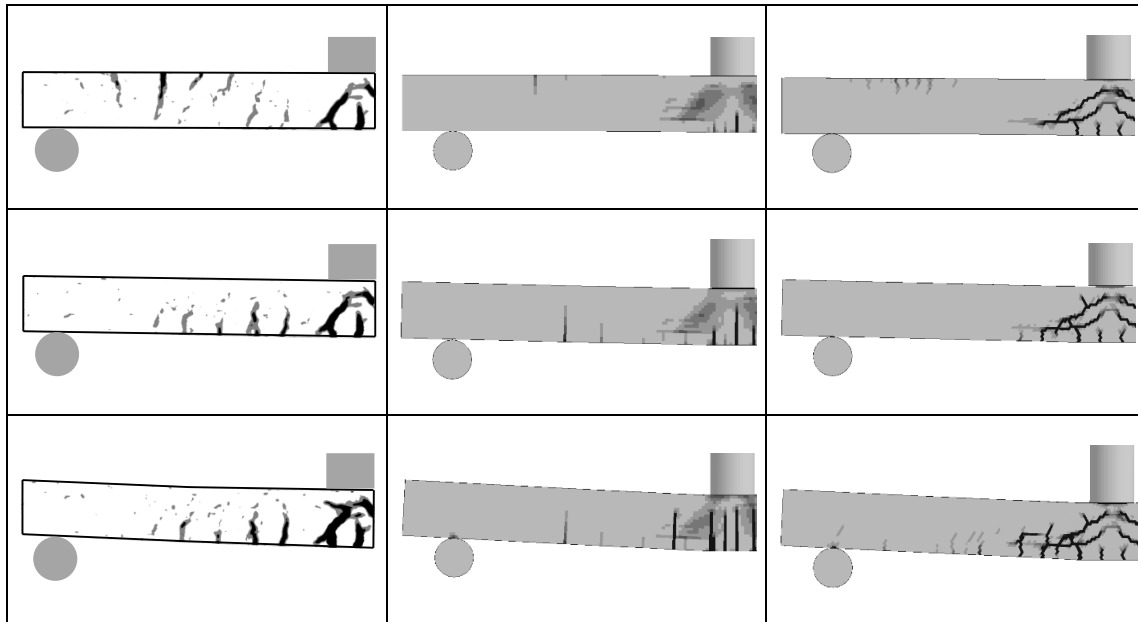(a)   (b)   c)
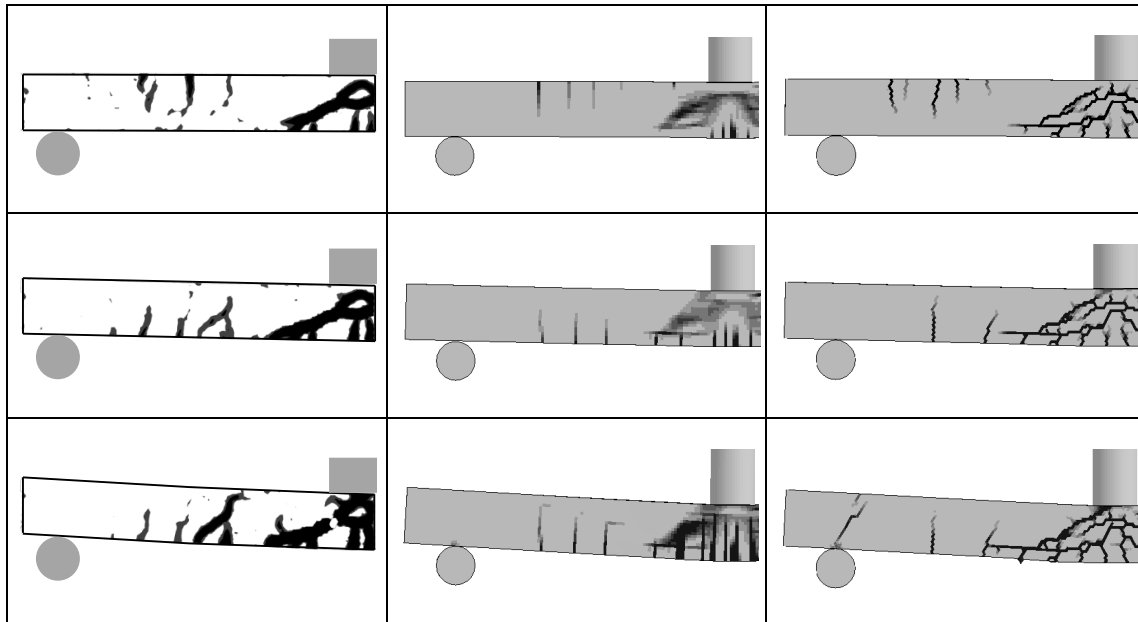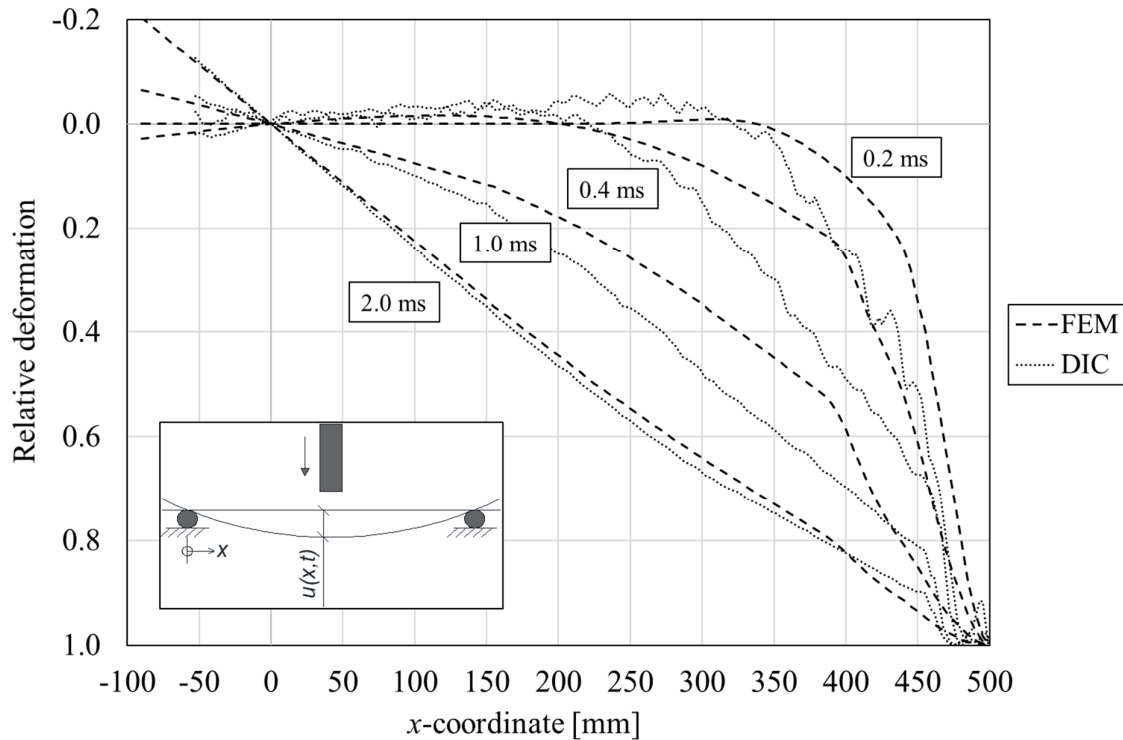
Fig. 7.   Comparison of DIC (dashed line in Fig. 6a) and FE-analyses for RC beam. (a) DIC, (b) hexahedral elements, and (c) tetrahedral elements. Time from impact: first row after 0.6 ms; second row after 2 ms; and third row after 9 ms.

Similar analyses were carried out for the FRC beams (Fig. 8). The response was very similar to the responses of the RC beams. However, the crack widths obtained using FRC are smaller than in the RC beam, both in the experiments and in the FE analysis. In the FE analysis, the early stage cracking is accurately captured (same concept as for RC shown in Fig. 7).

454

(a)   (b)   c)

Fig. 8.   Comparison of DIC (dashed line in Fig. 6b) and FE-analyses for FRC beam. (a)

DIC, (b) hexahedral elements, and (c) tetrahedral elements. Time from impact:

first row after 0.6 ms; second row after 2.0 ms; and third row after 8.0 ms.

The numerical analyses of the hexahedral elements show that the crack tend to follow the mesh

and that the diagonal shear cracks cannot be captured as well as with tetrahedral elements.

Initially, bending cracks form at the bottom of the beam and shear cracks form close to the

impact point. Then, bending cracks form at the top of the beam at a distance of roughly one-

fourth of the span length from the support. The appearance of bending cracks at the top of the

beam is due to wave propagation effects as schematically shown if Fig. 1. In Fig. 9, the relative

deformation, $u_{rel}(x,t) = u_{mod}(x,t)/u_{max}$, from DIC and FE analyses using hexahedral elements in

the RC beam is compared for the first 2 ms of loading. In the initial stage, the beam lifts at the

supports.   This   effect,   however,   has   been   negated   in   Fig. 9   by   setting

$u_{mod}(x,t) = u(x,t) - u_{support}(t)$. The relative deformation along the beam shows that the beam has

very high positive curvature beneath the drop weight and a negative curvature at the top soon

470   after impact. After the first two milliseconds, the deformed shape of the beam approaches that

471   of a simply supported beam subjected to a static point load, with a plastic hinge in the middle

472   of the beam. The relative deformation can be captured very effectively both in the DIC and the

473   FE analyses and corresponds well with that shown in Fig. 1.

474

Fig. 9.   Relative deformation for RC. Comparison with DIC (dashed line in Fig. 6a) and

476   FE analyses (hexahedral elements) for the first 2 ms after impact.

477   Based on the observations made above, it can be concluded that the FE model using tetrahedral

478   elements effectively reproduces the results obtained in the experiments both for RC and FRC

479   beams. Accordingly, it is also possible to use the FE analyses to further complement the

480   experiments; that is, they can be used to study different settings or phenomena that otherwise

481   may be difficult to study using experiments alone. The influence of different boundary

482   conditions, the impact force, the support reactions, and the strain localisation in the

483   reinforcement were studied using only FE analysis.

484   The effect of different boundary conditions was studied with FEM for the RC beam using

485   tetrahedral elements. The beams were supported on rollers – one beam was unrestrained and

486   the other beam had an upper restraint to prevent upward movements at the support (Fig. 10).


(a)   (b)
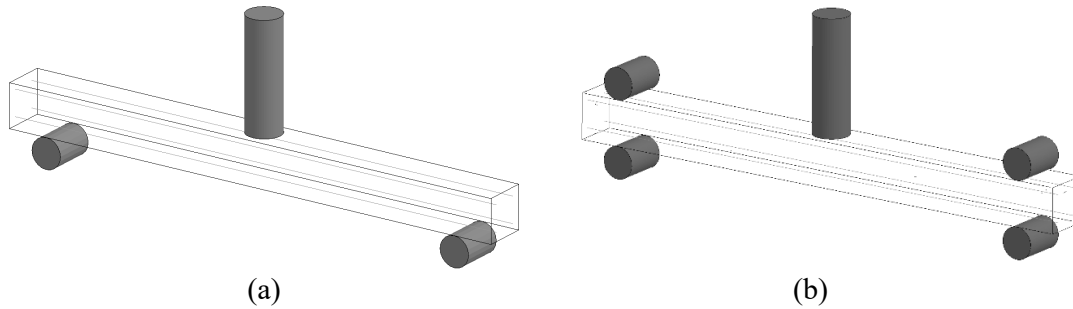
487   **Fig. 10.**   Numerical models used in FE analyses for study boundary conditions (a)

488   unrestrained beam (same model as in Fig. 5), and (b) restrained beam.

489   The deflections from the FE analyses at the support and the midpoint deflection for the

490   boundary conditions with and without upper restrain are compared in Fig. 11. In Fig. 11 (a), the

491   beam deflections, in the initial contact point between bottom roller and the beam, at the bottom

492   support are compared; in Fig. 11 (b), the midpoint deflections at the top of the beam for the two

493   models are compared. The results show that the behaviour of the beam is hardly affected by the

494   upper restraint for the first 15 ms, which is the time when the beams start to lift from their

495   supports and the midpoint deflections start to deviate, after approximately 17 ms. These results

496   show that the effect of the upper restrain has negligible effect on the midpoint deflection before

497   rebounding occurs even if the unrestrained beam initially lifted from the supports for a few

498   milliseconds. In addition, the restrained beam seems to have a small deflection at the support,

499   but this deflection is due to the rotation of the beam at the support – i.e., the beam is in contact

500   with the support at all times.
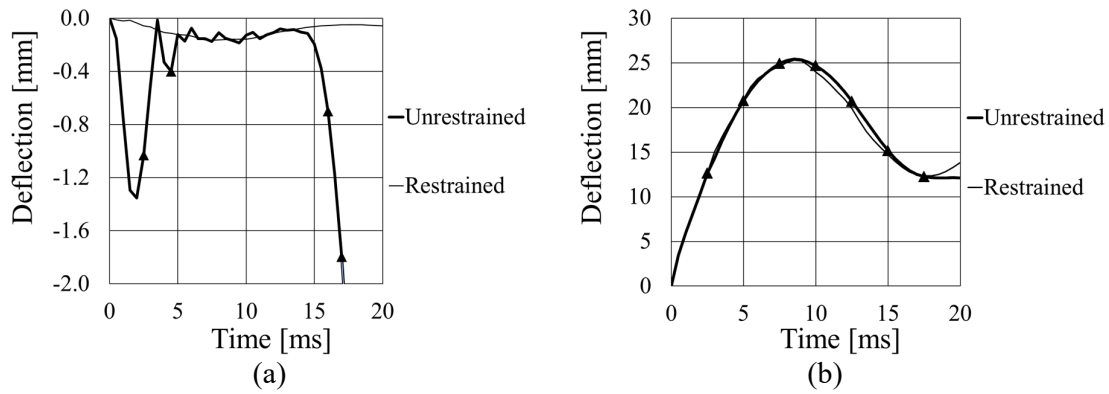
Fig. 11. Comparison of deflections with FE analyses with different boundary conditions (a) at the support, and (b) midpoint deflections. Positive direction is downwards.

The effect on crack propagation due to different boundary conditions is compared in Fig. 12. As the crack propagation is very similar and independent of boundary conditions, the upper restraint had very little effect on the crack propagation for the first 15 ms – i.e., the time when the unrestrained beam started to lift from its supports. The boundary condition may affect the response of the rebounded beam. However, the boundary condition has negligible effect on the response up to the maximum midpoint deflection in the direction of the applied load, which often causes the most damage for the beam.

510
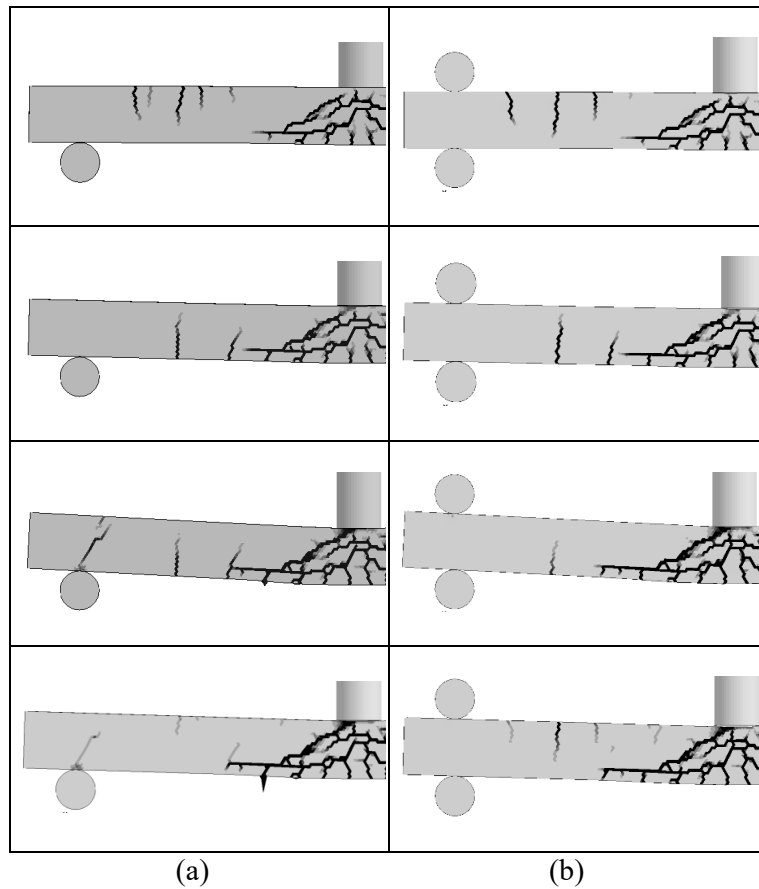
Fig. 12. Comparison of FE analyses for RC beam: (a) unrestrained beam, and (b) restrained beam. Time from impact: first row after 0.6 ms; second row after 2.0 ms; third row after 9 ms; and fourth row after 15 ms.

The force and impulse from the impact and support reaction, taken from the FE analyses with tetrahedral meshes, are shown in Fig. 13. At 0.1 ms after the impact, the magnitude of the impact force was very similar for the RC and FRC beams with peak values of 261 kN and 263 kN, respectively. The support reactions were also very similar: peak values of 224 kN (RC) and 222 kN (FRC). The delayed appearances of the support reactions, 3.4 ms (RC) and 3.0 ms (FRC), were due to a combination of wave propagation effects and the initial uplift of the beams at the supports; compare with Fig. 11 (a). The development of the impulses of the impact and support reaction is presented until a time corresponding to maximum deflection, reaching 104 Ns for the impact force and 101 Ns for the support reaction. The same values were obtained

26

523   for RC and FRC beams and can be compared to the momentum of the dead-weight just prior to

524   impact: $p_0 = m \cdot v = 10.1 \cdot 10.35 = 105$ Ns.
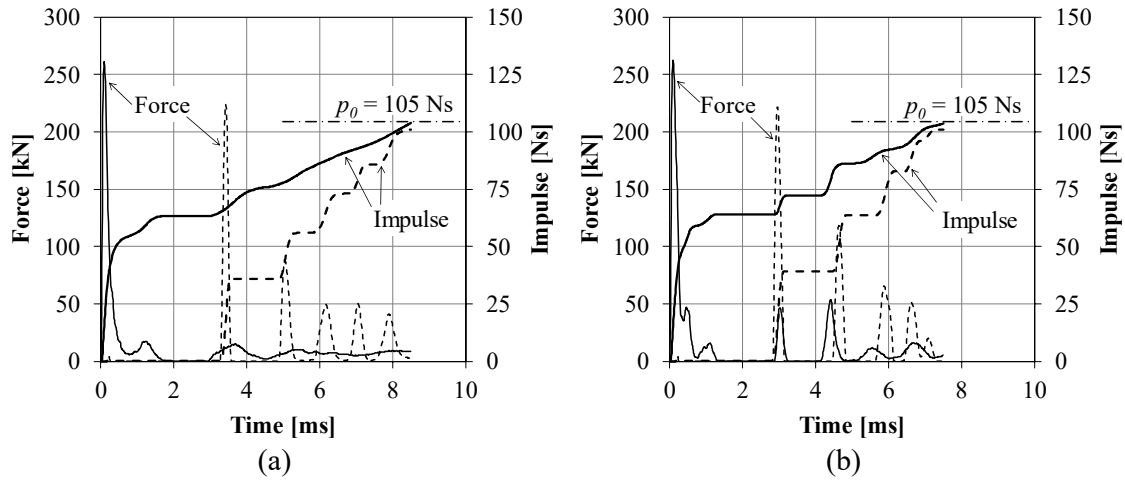

525   **Fig. 13.**   Force and impulse from impact force (solid lines) and total support reaction

526   (dashed lines) from FE analyses using tetrahedral elements of (a) RC beam and (b) FRC beam.

527   The momentum p_0 of the drop weight just prior to impact is marked as comparison. Impact or

528   support reaction forces were not measured in the experiments.

529   Fig. 14 shows strains in the reinforcement along the length of the RC and FRC beams. Although

530   the total deflection in the RC beam was larger than in the FRC beam, the maximum

531   reinforcement strain in the FRC beam was more than twice as high as in the RC beam. In the

532   RC beam, the maximum reinforcement strain did not exceed 25 ‰, and the strains were rather

533   evenly distributed in the middle of the beam, giving rise to a well-defined plastic hinge with a

534   length l_{pl} of approximately 0.35 m (l_{pl} is here defined as the total distance where $\varepsilon_s \geq 10$ ‰).

535   However, for the FRC beam, the maximum reinforcement strain reached 50 ‰, and the length

536   of its plastic hinge was considerably smaller, about 0.20 m.

537   The difference in response observed is due to different interaction between reinforcement and

538   concrete in the two models. In the RC beam, the strain in the reinforcement damages

539   surrounding concrete; i.e., spalling cracks appear that reduce the interaction stiffness between

27

540   reinforcement and concrete. This phenomenon enables the reinforcement strain to be more

541   evenly distributed over a longer distance, resulting in a more uniform strain distribution over a

542   larger length. In the FRC beam, the fibres make the concrete much more ductile; its fracture

543   energy is almost 15 times higher than that of the RC beam. Because the fibres prevent spalling

544   cracks from forming, the effective bond between reinforcement and concrete remains more or

545   less intact. A stiffer bond interaction leads to an increased amount of strain localisation, and

546   therefore the maximum reinforcement strain becomes higher. This increase is also evident in

547   Fig. 14 and has previously been observed for statically-loaded beams subjected to bending

548   failure [86,87].

549

550
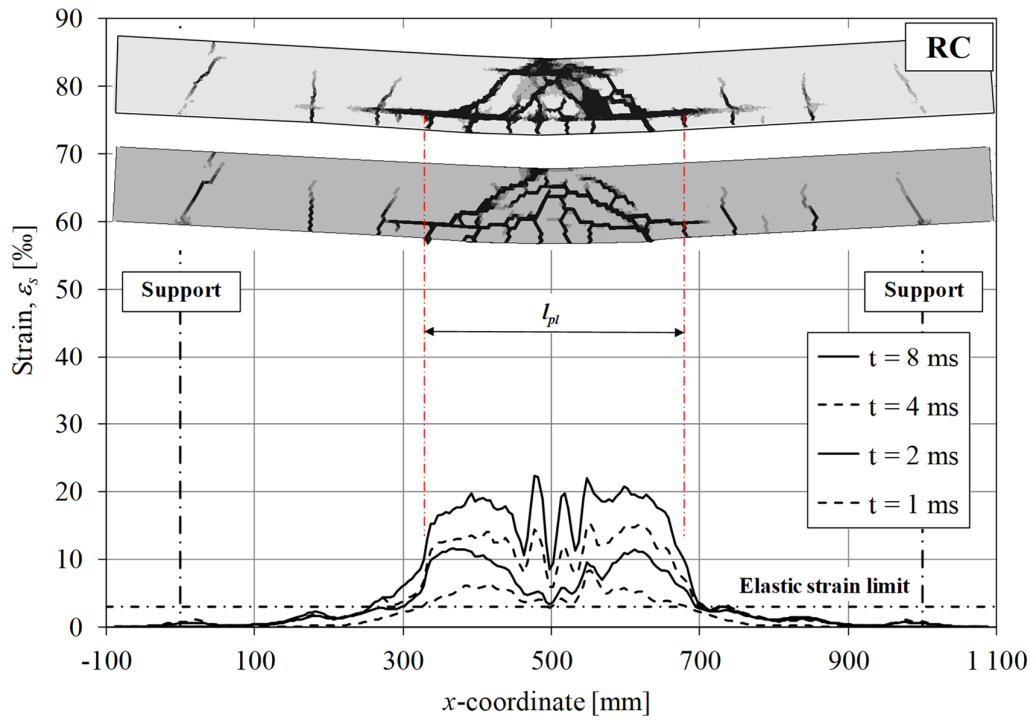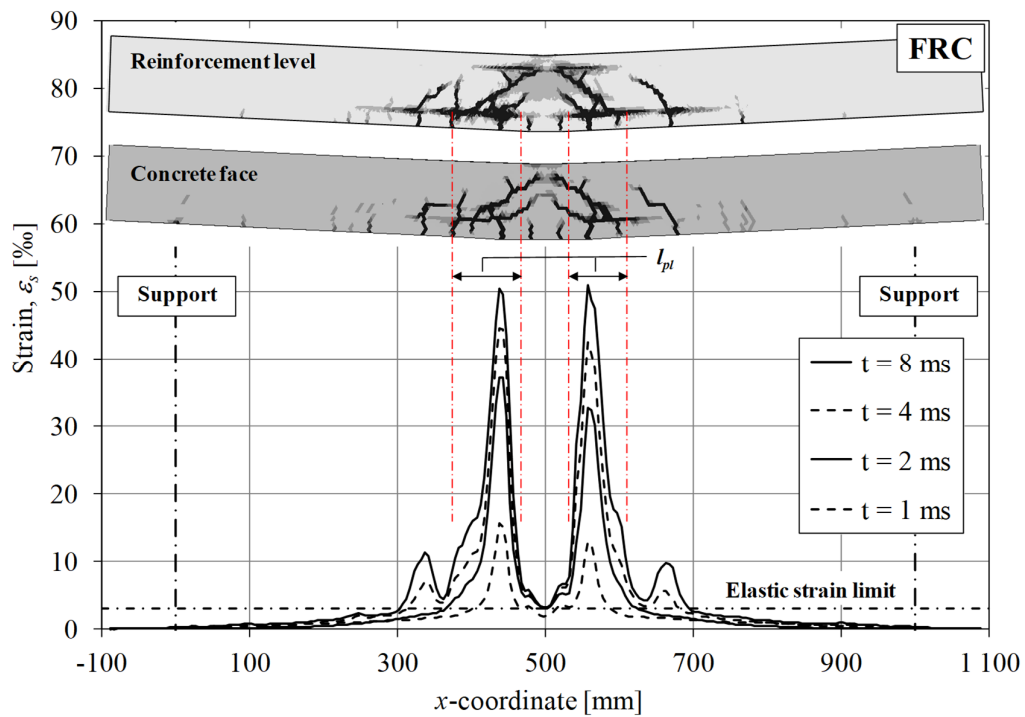
Fig. 14. Strain in bottom reinforcement in FE analyses of RC (top) and FRC (bottom) beams using tetrahedral elements. As comparison, the crack patterns obtained at the reinforcement level and at the concrete face are shown.

554　　In Section 1, it is concluded that the design of concrete structures subjected to impulse loading

555　　needs to make sure that the structure can manage large plastic deformations prior to failure.

556　　There are many parameters that affect the plastic deformation capacity of a reinforced concrete

557　　structure (e.g., reinforcement ductility (strength ratio f_u/f_y and ultimate strain), bond between

558　　reinforcement and concrete, mechanical reinforcement ratio, and structure slenderness); how to

559　　predict plastic deformation capacity is its own research field [88–90]. However, one important

560　　criterion for obtaining this response is to obtain a large plastic hinge in which the reinforcement

561　　can develop plastic strains. Whether the reinforcement or the concrete is critical for the final

562　　plastic deformation capacity depends on the reinforcement's mechanical properties and the

563　　mechanical reinforcement ratio. Low reinforcement ductility, high concrete strength and low

564　　reinforcement amount increase the risk of reinforcement rupture (Fig. 15). Hence, the

565　　observation made above is important, since it indicates that the maximum reinforcement strain

566　　in reinforced concrete structures may increase due to the presence of fibres – i.e., the risk of

567　　reinforcement rupture may increase. Depending on the configuration of the structure, this may

568　　have considerable negative effects on the structure's deformation capacity. In this study, the

569　　deformation capacities proved to be adequate for both the RC and the FRC beams. However,

570　　in a structure with smaller mechanical reinforcement amount, there is increased risk for ruptured

571　　reinforcement leading to collapse.
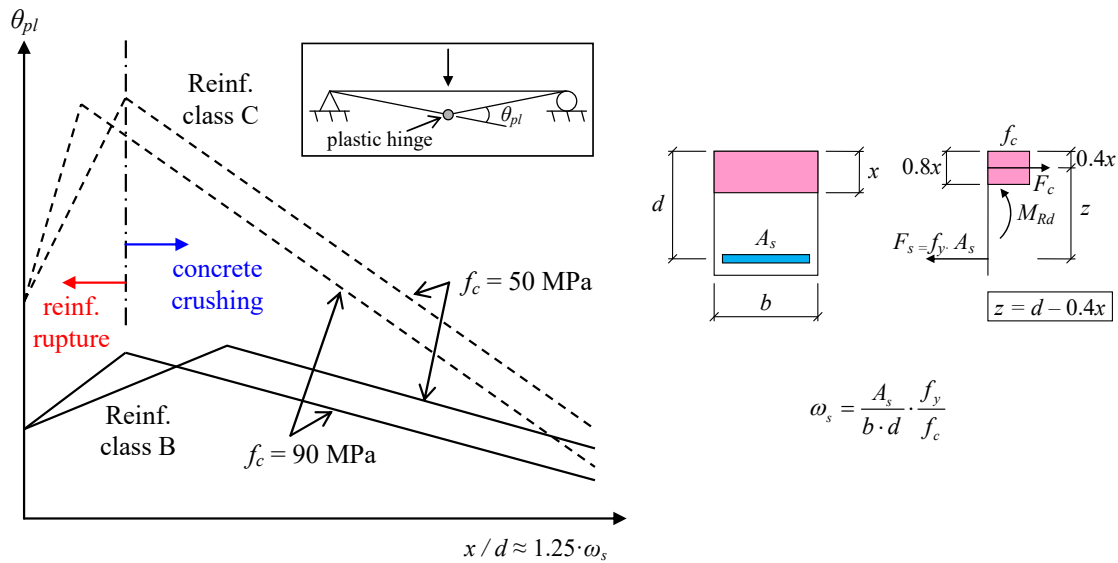
Fig. 15. Schematic illustration of plastic deformation as function of the mechanical reinforcement ratio ω_s for different classes of reinforcement (class C is more ductile than class B) and concrete strength. For each line, the ascending and descending branch indicates reinforcement rupture and concrete crushing, respectively. Based on [71].

In the FE models used here, perfect bond between reinforcement and concrete was assumed. Hence, the bond-slip relation between reinforcement and surrounding concrete was not explicitly incorporated in the model. Nevertheless, the effect of reduced bond is still included in an approximate way since the concrete in the vicinity of the reinforcement bars are affected (cracked) by the force in the reinforcement. In Fig. 14, the effect of reduced bond is indicated by the horizontal cracks at the level of the bottom reinforcement - i.e., spalling cracks. The extension of this zone of reduced bond also agrees well with the location of large reinforcement strains in both the RC and the FRC beam.

5. Conclusions

Based on experiments and numerical analyses of drop weight impact tests of RC and FRC beams, the following conclusions can be drawn.

31

587   Digital image correlation (DIC) analysis of high-speed camera images is a very powerful tool

588   for analysing the response of drop weight impact tests. The deformation and crack propagation

589   of the beams tested could be followed in detail.

590   FE analyses with the material model CDPM2, using tetrahedral elements, effectively captures

591   the response of the impact loaded beams. The use of hexahedral elements is not adequate for

592   representing correct response when diagonal cracks are formed.

593   The FE analyses showed that the strains in the reinforcement were more evenly distributed and

594   that the length of the plastic hinge was larger in the RC beams than for FRC beams. In the latter,

595   larger maximum strains were also obtained, even though both deflection and crack widths were

596   smaller in the experiments. This finding indicates that there may be an increased risk of

597   reinforcement rupture in FRC structures, a finding that calls for further study.

598   The CDPM2 material model shows promising results for use in the evaluation of impulse loaded

599   structures; however, there is need for further investigating into how to model the influence of

600   strain rates on concrete properties in general and, in particular on fracture energy.

References

[1]   P.H. Bischoff, S.H. Perry, Compressive behaviour of concrete at high strain rates, Mater. Struct. 24 (1991) 425–450.

[2]   L.J. Malvar, C.A. Ross, Review of strain rate effects for concrete in tension, ACI Mater. J. 95 (1998) 735–739.

[3]   L.J. Malvar, Review of Static and Dynamic Properties of Steel Reinforcing Bars, ACI Mater. J. 95 (1998).

[4]   A. Miyamoto, M. King, M. Fujii, Non-linear dynamic analysis and design concepts for RC beams under implusive loads, Bull. New Zeal. Soc. Earthq. Eng. 22 (1989) 98–111.

[5]   K. Fujikake, T. Senga, N. Ueda, T. Ohno, M. Katagiri, Study on Impact Response of Reactive Powder Concrete Beam and Its Analytical Model, J. Adv. Concr. Technol. - J ADV CONCR TECHNOL. 4 (2006) 99–108.

[6]   D.M. Cotsovos, N.D. Stathopoulos, C.A. Zeris, Behavior of RC Beams Subjected to High Rates of Concentrated Loading, J. Struct. Eng. 134 (2008) 1839–1851.

[7]   X.X. Zhang, A.M. Abd Elazim, G. Ruiz, R.C. Yu, Fracture behaviour of steel fibre-reinforced concrete at a wide range of loading rates, Int. J. Impact Eng. 71 (2014) 89–96.

[8]   K. Fujikake, B. Li, S. Soeun, Impact Response of Reinforced Concrete Beam and Its Analytical Evaluation, J. Struct. Eng. 135 (2009) 938–950.

[9]   W.-J. Yi, D.-B. Zhao, S.K. Kunnath, Simplified Approach for Assessing Shear Resistance of Reinforced Concrete Beams under Impact Loads., ACI Struct. J. 113 (2016) 747.

632 [10] P. Isaac, A. Darby, T. Ibell, M. Evernden, Experimental investigation into the force

633   propagation velocity due to hard impacts on reinforced concrete members, Int. J.

634   Impact Eng. 100 (2017) 131–138.

635 [11] G.S.D. Ulzurrun, C. Zanuy, M. Johansson, R. Rempling, Impact propagation effects

636   along reinforced concrete beams, in: IABSE Symp. Guimarães 2019, Towar. a

637   Resilient Built Environ. - Risk Asset Manag. Guimarães, Port., 2019.

638 [12] J. Lovén, E.S. Svavarsdóttir, Concrete Beams Subjected to Drop Weight Impact,

639   Comparison of experimental data and numerical modelling, Chalmers University of

640   Technology, Department of Civil and Environmental Engineering, Göteborg, 2016.

641 [13] P. Grassl, M. Johansson, J. Leppänen, On the numerical modelling of bond for the

642   failure analysis of reinforced concrete, Eng. Fract. Mech. 189 (2018) 13–26.

643 [14] J.M. Biggs, Introduction to Structural Dynamics. McGraw-Hill, New-York, USA,

644   1964.

645 [15] D. Cormie, G. Mays, P. Smith, Blast Effects on Buildings, Second Edition. Thomas

646   Telford Ltd, London, UK, 2009.

647 [16] DOD, Structures to Resist the Effects of Accidental Explosions. UFC 3-340-02,

648   Department of Defence, USA, 2008.

649 [17] FKR, Swedish Fortifications Agency. Building Regulations FKR 2011. Dnr.

650   4535/2011 (In Swedish). Eskilstuna, Sweden, 2011.

651 [18] N. Kishi, H. Mikami, K.G. Matsuoka, T. Ando, Impact behavior of shear-failure-type

652   RC beams without shear rebar, Int. J. Impact Eng. 27 (2002) 955–968.

653 [19] S. Saatci, F.J. Vecchio, Effects of Shear Mechanisms on Impact Behavior of

654   Reinforced Concrete Beams., ACI Struct. J. 106(1) (2009) 78–86.

655 [20] J. Magnusson, M. Hallgren, A. Ansell, Shear in concrete structures subjected to

656   dynamic loads, Struct. Concr. 15 (2014) 55–65.

657 [21] K. Shivakumar, W. Elber, W. Illg, Prediction of Impact Force and Duration During

658   Low Velocity Impact On Circular Composite Laminates, J. Appl. Mech. Trans. ASME.

659   52 (1985).

660 [22] J. Mier, A. Pruijssers, H. Reinhardt, T. Monnier, Load-Time Response of Colliding

661   Concrete Bodies, J. Struct. Eng. 117 (1991) 354–374.

662 [23] T.M. Pham, H. Hao, Influence of global stiffness and equivalent model on prediction of

663   impact response of RC beams, Int. J. Impact Eng. 113 (2018) 88–97.

664 [24] H. Li, W. Chen, H. Hao, Dynamic response of precast concrete beam with wet

665   connection subjected to impact loads, Eng. Struct. 191 (2019) 247–263.

666 [25] W. Zhao, J. Qian, P. Jia, Peak Response Prediction for RC Beams under Impact

667   Loading, Shock Vib. 2019 (2019) 1–12.

668 [26] M. Johansson, L. Laine, Bebyggelsens motståndsförmåga mot extrem dynamisk

669   belastning Del 3: Kapacitet hos byggnader, (The resistance of housing settlement

670   subjected to extreme dynamic loading. Part 3: Building capacity. In Swedish), 2012.

671 [27] L. Ågårdh, K.G. Bolling, L. Laine, Fibre reinforced concrete beams loaded by impact,

672   Experiments and FE-modelling, Defence research establishment, FOA-R--9700587-

673   311--SE, Tumba, Sweden, 1997.

674 [28] S. Tachibana, H. Masuya, S. Nakamura, Performance based design of reinforced

675   concrete beams under impact, Nat. Hazards Earth Syst. Sci. 10 (2010) 1069–1078.

676 [29] S.M.M. Soleimani, N. Banthia, A Novel Drop Weight Impact Setup for Testing

677   Reinforced Concrete Beams, Exp. Tech. 38 (2014) 72–79.

678   [30]   S. Das Adhikary, B. Li, K. Fujikake, Dynamic behavior of reinforced concrete beams

679   under varying rates of concentrated loading, Int. J. Impact Eng. 47 (2012) 24–38.

680   [31]   G.S.D. Ulzurrun, C. Zanuy, Enhancement of impact performance of reinforced

681   concrete beams without stirrups by adding steel fibers, Constr. Build. Mater. 145

682   (2017) 166–182.

683   [32]   B. Barr, A. Bouamrata, Development of a repeated dropweight impact testing

684   apparatus for studying fibre reinforced concrete materials, Composites. 19 (1988) 453–

685   466.

686   [33]   X.X. Zhang, G. Ruiz, R.C. Yu, A New Drop-Weight Impact Machine for Studying

687   Fracture Processes in Structural Concrete, Strain. 46 (2008) 252–257.

688   [34]   X.X. Zhang, A.M. Abd Elazim, G. Ruiz, R.C. Yu, Fracture behaviour of steel fibre-

689   reinforced concrete at a wide range of loading rates, Int. J. Impact Eng. 71 (2014) 89–

690   96.

691   [35]   P.L. Reu, T.J. Miller, The application of high-speed digital image correlation, J. Strain

692   Anal. Eng. Des. 43 (2008) 673–688.

693   [36]   J. Ekström, Blast and Impact Loaded Concrete Structures - Numerical and

694   Experimental Methodologies for Reinforced Plain and Fibre Concrete Structures,

695   Chalmers University of Technology, 2017.

696   [37]   L.J. Malvar, J.E. Crawford, J.W. Wesevich, D. Simons, A plasticity concrete material

697   model for DYNA3D, Int. J. Impact Eng. 19 (1997) 847–873.

698   [38]   L.E. Schwer, Y.D. Murray, A three-invariant smooth cap model with mixed hardening,

699   Int. J. Numer. Anal. Methods Geomech. 18 (1994) 657–688.

700   [39]   L.F. Pereira, J. Weerheijm, L.J. Sluys, A numerical study on crack branching in quasi-

brittle materials with a new effective rate-dependent nonlocal damage model, Eng. Fract. Mech. 182 (2017) 689–707.

[40]   L.F. Pereira, J. Weerheijm, L.J. Sluys, Simulation of compaction and crushing of concrete in ballistic impact with a new damage model, Int. J. Impact Eng. 111 (2018) 208–221.

[41]   N. Gebbeken, M. Ruppert, A new material model for concrete in high-dynamic hydrocode simulations, Arch. Appl. Mech. (Ingenieur Arch. 70 (2000) 463–478.

[42]   P. Grassl, M. Jirásek, Damage-plastic model for concrete failure, Int. J. Solids Struct. 43 (2006) 7166–7196.

[43]   J. Lee, G.L. Fenves, Plastic-Damage Model for Cyclic Loading of Concrete Structures, J. Eng. Mech. 124 (1998) 892–900.

[44]   J. Lubliner, J. Oliver, S. Oller, E. Oñate, A plastic-damage model for concrete, Int. J. Solids Struct. 25 (1989) 299–326.

[45]   H. Othman, H. Marzouk, Applicability of damage plasticity constitutive model for ultra-high performance fibre-reinforced concrete under impact loads, Int. J. Impact Eng. 114 (2018) 20–31.

[46]   J. Ožbolt, A. Sharma, H.-W. Reinhardt, Dynamic fracture of concrete – compact tension specimen, Int. J. Solids Struct. 48 (2011) 1534–1543.

[47]   J. Ožbolt, A. Sharma, Numerical simulation of reinforced concrete beams with different shear reinforcements under dynamic impact loads, Int. J. Impact Eng. 38 (2011) 940–950.

[48]   J. Feng, W. Yao, W. Li, W. Li, Lattice discrete particle modeling of plain concrete perforation responses, Int. J. Impact Eng. 109 (2017) 39–51.

724   [49]   K. Kim, J.E. Bolander, Y.M. Lim, Failure simulation of RC structures under highly

725   dynamic conditions using random lattice models, Comput. Struct. 125 (2013) 127–136.

726   [50]   K.-J. Bathe, Finite Element Procedures. Prentice Hall, Englewood Cliffs, New Jersey,

727   USA, 1996.

728   [51]   P. Grassl, D. Xenos, U. Nyström, R. Rempling, K. Gylltoft, CDPM2: A damage-

729   plasticity approach to modelling the failure of concrete, Int. J. Solids Struct. 50 (2013)

730   3805–3816.

731   [52]   P. Grassl, U. Nyström, R. Rempling, K. Gylltoft, A damage-plasticity model for the

732   dynamic failure of concrete, in: Proc. 8th Int. Conf. Struct. Dyn. EURODYN 2011,

733   2011: pp. 4–6.

734   [53]   B. İrhan, J. Ožbolt, D. Ruta, 3D finite element simulations of high velocity projectile

735   impact, Int. J. Solids Struct. 72 (2015) 38–49.

736   [54]   W. Luo, V.T. Chau, Z.P. Bažant, Effect of high-rate dynamic comminution on

737   penetration of projectiles of various velocities and impact angles into concrete, Int. J.

738   Fract. 216 (2019) 211–221.

739   [55]   R. Shao, C. Wu, Y. Su, Z. Liu, J. Liu, S. Xu, Numerical analysis on impact response of

740   ultra-high strength concrete protected with composite materials against steel ogive-

741   nosed projectile penetration, Compos. Struct. 220 (2019) 861–874.

742   [56]   A. Nishida, Z. Kang, M. Nagai, H. Tsubota, Y. Li, Evaluation of local damage to

743   reinforced concrete panels subjected to oblique impact by soft missile, Nucl. Eng. Des.

744   350 (2019) 116–127.

745   [57]   R. Hosseinzadeh, M.M. Shokrieh, L. Lessard, Damage behavior of fiber reinforced

746   composite plates subjected to drop weight impacts, 66 (2006) 61–68.

747 [58] L. Schwer, Prediction of Air Blast Loaded Concrete Slab Response Using Six LS-

748   DYNA Concrete Models. Tech. rep., pp. 1-32, 2013.

749 [59] M. Jirásek, P. Grassl, Evaluation of directional mesh bias in concrete fracture

750   simulations using continuum damage models, Eng. Fract. Mech. 75 (2008) 1921–1943.

751 [60] J.G. Rots, Computational modeling of concrete fracture, Delft University of

752   Technology, 1988.

753 [61] P. Grassl, Quasi-static three point bending LS-Dyna analyses with MAT CDPM (MAT

754   273) using tetra- and hexahedral meshes., Research report, School of Engineering,

755   University of Glasgow, 2016.

756 [62] Q. Fang, J. Zhang, Three-dimensional modelling of steel fiber reinforced concrete

757   material under intense dynamic loading, Constr. Build. Mater. 44 (2013) 118–132.

758 [63] J. Ožbolt, J. Bošnjak, E. Sola, Dynamic fracture of concrete compact tension specimen:

759   Experimental and numerical study, Int. J. Solids Struct. 50 (2013) 4270–4278.

760 [64] G. Ruiz, A. Pandolfi, M. Ortiz, Three-dimensional cohesive modeling of dynamic

761   mixed-mode fracture, Int. J. Numer. Methods Eng. 52 (2001) 97–120.

762 [65] F.J. Lozano, J.A. Makdesi, Concrete Beams Subjected to Drop-Weight Impact and

763   Static Load: Structural Behavior and Plastic Rotational Capacity from Experiments and

764   Finite Element Analysis, Chalmers University of Technology, 2017.

765 [66] Software ARAMIS., (n.d.). http://www.gom.com/3d-software/gom-correlate.html

766   (accessed June 25, 2018).

767 [67] CEN 2004, EN 12390-3: Testing hardened concrete - Part 3: Compressive strength of

768   test specimens, 2009.

769   [68]   CEN 2004, EN 12390-6: Testing hardened concrete - Part 6: Tensile splitting strength

770   of test specimens, 2009.

771   [69]   I. Löfgren, J.F. Olesen, M. Flansbjer, Application of WST-method for fracture testing

772   of fibre- reinforced concrete, Chalmers University of Technology, Department of

773   Structural Engineering and Mechanics, Report 04:13, 2004.

774   [70]   RILEM TC 162-TDF. Brite Euram Project nr: BE 97-4163, Test and Design Methods

775   for Steel Fibre Reinforced Concrete, ISBN 90-5682-358-2, June, 2002.

776   [71]   CEN, EN 1992-1-1, Design of concrete structures - Part 1-1: General rules and rules

777   for buildings, (2004).

778   [72]   M. Jirásek, Z.P. Bažant, Inelastic analysis of structures., John Wiley and Sons,

779   Chichester, 2002.

780   [73]   P. Menétrey, K.J. Willam, A triaxial failure criterion for concrete and its

781   generalization, ACI Struct. J. 92 (1995) 311–318.

782   [74]   P. Ladeveze, A damage computational approach for composites: Basic aspects and

783   micromechanical relations, Comput. Mech. 17 (1995) 142–150.

784   [75]   U. Häussler-Combe, T. Kühn, Modeling of strain rate effects for concrete with

785   viscoelasticity and retarded damage, Int. J. Impact Eng. 50 (2012) 17–28.

786   [76]   T. Li Piani, J. Weerheijm, L.J. Sluys, Dynamic simulations of traditional masonry

787   materials at different loading rates using an enriched damage delay: theory and

788   practical applications, Eng. Fract. Mech. 218 (2019) 21.

789   [77]   G. Cusatis, Strain-rate effects on concrete behavior, Int. J. Impact Eng. 38 (2011) 162–

790   170.

791 [78] CEB, CEB-FIB Model Code 1990. Design Code, Thomas Telford, Lausanna,

792 Switzerland, 437 pp, 1993.

793 [79] Z.P. Bažant, B. Oh, Crack band theory for fracture of concrete, Mater. Struct. 16

794 (1983).

795 [80] S.T. Pietruszczak, Z. Mróz, Finite element analysis of deformation of strain-softening

796 materials, 1981.

797 [81] K. Willam, N. Bićanić, S. Sture, Composite fracture model for strain-softening and

798 localised failure of concrete, in: E. Hinton, D.R.J. Owen (Eds.), Comput. Model. Reinf.

799 Concr. Struct., Pineridge Press, Swansea, 1986: pp. 122–153.

800 [82] M. Jirásek, M. Bauer, Numerical aspects of the crack band approach, Comput. Struct.

801 110–111 (2012) 60–78.

802 [83] G.R. Johnson, W.H. Cook, Fracture characteristics of three metals subjected to various

803 strains, strain rates, temperatures and pressures, Eng. Fract. Mech. 21 (1985) 31–48.

804 [84] CEB, Concrete Structures under Impact and Impulsive Loading. CEB Bulletin

805 d'Information No 187, Lausanne, Switzerland, 1988.

806 [85] LS-DYNA., (n.d.). http://www.lstc.com/ (accessed June 25, 2018).

807 [86] A. Meda, F. Minelli, G.A. Plizzari, Flexural behaviour of RC beams in fibre reinforced

808 concrete, Compos. Part B Eng. 43 (2012) 2930–2937.

809 [87] C.G. Berrocal, I. Löfgren, K. Lundgren, The effect of fibres on steel bar corrosion and

810 flexural behaviour of corroded RC beams, Eng. Struct. 163 (2018) 409–425.

811 [88] CEB, Ductility of Reinforced Concrete Structures. CEB Bulletin d'information No

812 242, Lausanne, Switzerland, 1998.

813   [89]   Bigaj A.J., Structural Dependence of Rotational Capacity of Plastic Hinges in RC

814   Beams and Slabs, TU Delft, Civil Engineering and Geosciences, Delft, The

815   Netherlands, 1999.

816   [90]   Plem E., The Rotational Capacity of Plastic Hinges in Reinforced Concrete Beams: A

817   Theoretical Study. Lund Institute of Technology, Department of Structural Mechanics,

818   Vol. R81-1, Lund, Sweden, 1981.

819 **Appendix**

820 **Table A.1**

821 Data summary for the self-compacting concrete mixtures.

	Plain	Fibre reinforced
Constituents	Amount [kg/m^3]	Amount [kg/m^3]
Cement	335	335
Limestone filler	160	160
Sand	747.3	741.1
Aggregates		
4 – 8 mm	268.9	266.8
8 – 16 mm	717.1	711.4
Superplasticiser	5.36	5.36
Fibre	-	40
Water	184.3	184.3
w-c ratio	0.55	0.55

822

823 **Table A.2**

824 Geometry for the drop weight.

Length	260 [mm]
Diameter	80 [mm]
Weight	10.1 [kg]
Radius of the head	400 [mm]

825
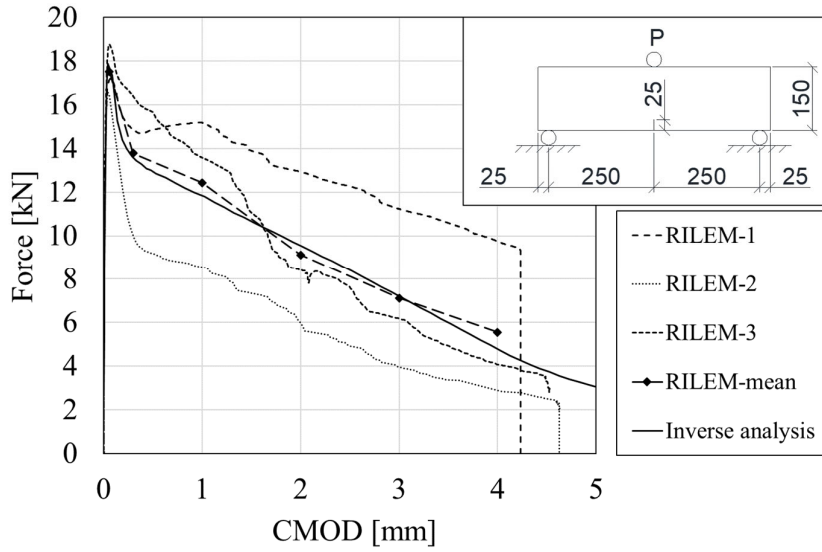
Fig. A.1. Force – CMOD curve from RILEM beams, and results from adaptive inverse

analysis.

828
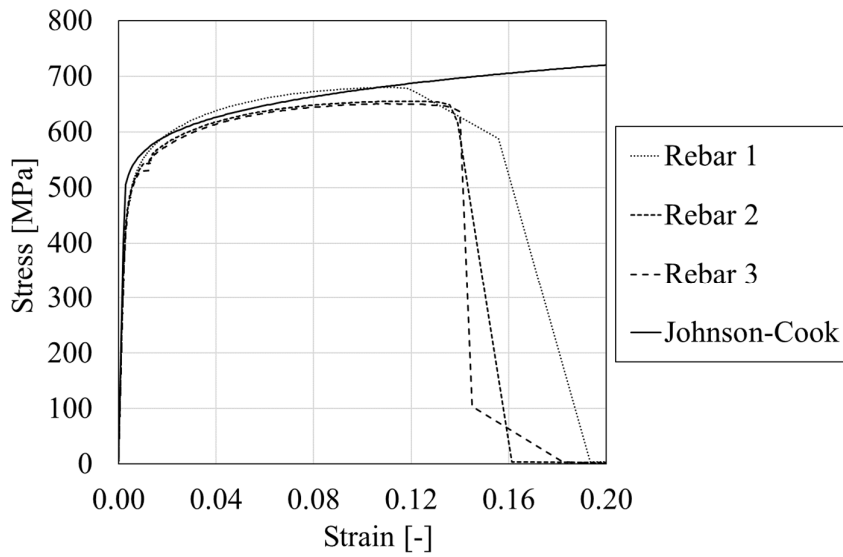
Fig. A.2. Stress-strain curve for the reinforcement: measured values (3 bars) vs. input data

to FE analyses for the material model Johnson-Cook.